RSC Advances

PAPER

View Article Online
View Journal | View Issue

Cite this: *RSC Adv.*, 2025, **15**, 28853

Eco-friendly and recyclable ionic liquid–zinc chloride catalyst supported on graphene oxide from *Nypa fruticans* husk for green synthesis of 2-amino-3-cyanopyridine derivatives

Y.-Nhi Thi Nguyen,†[ab] Dat Minh Tran,†[ab] Thai The Nguyen[bc] and Hai Truong Nguyen *[ab]

This study successfully demonstrates the application of GO/IL/Zn_xCl_y as a novel and environmentally friendly catalyst for the synthesis of 2-amino-3-cyanopyridine derivatives. Using *Nypa fruticans* husk as a precursor, a hybrid catalyst combining graphene oxide (GO), ionic liquid (IL), and zinc chloride-based species ($Zn_xCl_y^-$) was produced, exhibiting higher catalytic activity, better selectivity, and outstanding recyclability. The structural and morphological features of GO/IL/Zn_xCl_y were investigated using FT-IR spectroscopy, Raman spectroscopy, XRD analysis, ICP-MS analysis, scanning electron microscopy (SEM), energy-dispersive X-ray spectroscopy (EDX), and thermogravimetric analysis (TGA) to elucidate their properties and establish the catalyst's efficiency and stability in organic synthesis. Under solvent-free conditions, we investigated the adaptability of the catalyst by effectively synthesizing of 2-amino-3-cyanopyridine derivatives with moderate to high yields (up to 57%), at 110 °C for 40 min. Analysis of the electronic and steric effects of different substituents revealed that electron-donating groups improve yield while electron-withdrawing groups reduce it, thereby offering insightful information for further catalyst modifications. The sustainability of the approach was determined by applying green chemistry criteria. The key indicators highlighting notable waste reduction and effective resource use were an E-factor of 1.40, an atom economy of 73.44%, and a process mass intensity (PMI) of 2.40. GO/IL/Zn_xCl_y provides a possible substitute for sustainable organic synthesis owing to its excellent catalytic efficiency, selectivity, recyclability, and eco-friendly nature.

Received 3rd July 2025
Accepted 9th August 2025

DOI: 10.1039/d5ra04734j

rsc.li/rsc-advances

1. Introduction

Scientists have been paying increasing attention to environmental issues in recent years due to severe pollution. Therefore, renewable resources such as biomass are considered potential alternatives to fossil fuels and chemicals. Developing innovative methods to convert biomass into materials for use as catalysts remains a significant challenge. Biomass is used as a feedstock to prepare carbon materials through carbonization processes (*e.g.*, pyrolysis and hydrothermal carbonization),[1] which have demonstrated significant potential in enhancing the efficiency of organic synthesis reactions.[2–4] The GO/IL–metal composite, which integrated graphene oxide (GO), ionic liquids (IL), and metal species, has emerged as a highly versatile material with significant potential in catalysis,[5,6] electrochemistry,[7,8] and environmental[9] remediation. The combination of three components (*e.g.* GO, IL, and metal halide) leads to enhanced stability, conductivity, dispersion, and reactivity, making the composite a highly promising candidate for various applications. The GO exhibits many characteristic properties such as high surface area, oxygen-containing functional groups, and electron transfer properties. These properties allow it to serve as a robust support material, ensuring the uniform dispersion of metal while preventing aggregation.[10] ILs act as stabilizing and structuring agents, offering high thermal and chemical stability, tunable solubility, and improved ion mobility, which further enhances catalytic performance.[11,12] The incorporation of metal species, whether transition metals like Fe, Cu, and Zn or noble metals like Au, Pt, and Pd, introduces redox activity and adsorption capabilities, making the material suitable for heterogeneous catalysis, electrocatalysis, and environmental applications.[13,14] The presence of these special components confers many superior properties, thereby highlighting this type of material.[15,16] Besides the advantages, this material faces challenges related to scalability, cost-effectiveness, and long-term stability.[17] While noble metals offer high catalytic

[a]*Department of Organic Chemistry, Faculty of Chemistry, University of Science, Ho Chi Minh City, 700000, Vietnam. E-mail: ngthai@hcmus.edu.vn; Tel: +84-908-108-824*
[b]*Vietnam National University, Ho Chi Minh City, 700000, Vietnam*
[c]*Faculty of Interdisciplinary Science, University of Science, Ho Chi Minh City, 700000, Vietnam*
† These authors contributed equally to this work.

efficiency, their cost limits large-scale applications, making the exploration of earth-abundant metals an important area of research. Additionally, preventing IL degradation and metal leaching over time is critical to maintaining long-term performance.[12,18,19]

Heterocyclic compounds are a wide range of structures with one or more rings in which heteroatoms are present (*e.g.* nitrogen, oxygen, and sulfur). The synthesis of N-heterocyclic compounds plays a vital role in organic synthesis, these compounds are used as pharmacophores in drug design,[20,21] including antibacterial, anticancer, antioxidant, and antiviral activities.[22–25] In the pharmaceutical field, drug candidates derived from pyridine derivatives are well-known for their promising biological properties. 2-Amino-3-cyanopyridine derivatives have attracted significant attention for their diverse biological profiles, including antibacterial,[26] anticancer,[27,28] and anti-tubercular properties.[29] Several methods have been developed for the synthesis of 2-amino-3-cyanopyridine derivatives. In 2014, P. N. Kalaria *et al.* described a method for synthesizing 2-amino-3-cyanopyridine derivatives by one-pot four-component reaction. This experiment involves the cyclization reaction of substituted 5-(1*H*-imidazol/4-methyl-1-yl)-3-methyl-1-phenyl-1*H*-pyrazole-4-carbaldehyde with malononitrile, ammonium acetate, and an aromatic/heterocyclic methyl ketone.[29] In 2019, L. Xu *et al.* reported a synthetic protocol for the preparation of 2-amino-3-cyanopyridines utilizing benzaldehyde, malononitrile, and ammonium acetate in toluene.[30] Additionally, in 2020, R. Sabour *et al.* reported the process of synthesizing amino cyanopyridines *via* a one-pot reaction from chalcones, malononitrile, and ammonium acetate in absolute ethanol.[31] Consequently, the development of efficient and eco-friendly synthetic techniques for 2-amino-3-cyanopyridine derivatives is highly desirable.

The aims of this study are to develop a novel synthesis approach for GO/IL/Zn_xCl_y using *Nypa fruticans* husk as a precursor to produce a catalyst for the synthesis of 2-amino-3-cyanopyridine derivatives. To evaluate the catalytic performance of GO/IL/Zn_xCl_y, a representative reaction was selected, involving arylaldehyde (1.0 mmol), acetophenone derivatives (1.0 mmol), ammonium acetate (1.5 mmol), and malononitrile (1.0 mmol) under solvent-free conditions. The outstanding properties of GO/IL/Zn_xCl_y enable an eco-friendly and efficient approach to 2-amino-3-cyanopyridine synthesis under mild conditions. Additionally, the catalyst's reusability and one-pot reaction align with green chemistry principles, making it a sustainable option for multi-component organic transformations.

2. Results and discussion

2.1. Catalyst characterization

This process was chosen to synthesize a functionalized graphene oxide-based material from *Nypa fruticans* husk-derived graphite using a systematic and efficient chemical modification approach (Scheme 1). The oxidation of graphite into graphene oxide (GO) was performed using the modified Hummers' method (using $KMnO_4$, $NaNO_3$, and H_2SO_4) under controlled conditions to achieve high oxidation efficiency. The reaction was carried out under acidic conditions to form oxygen-

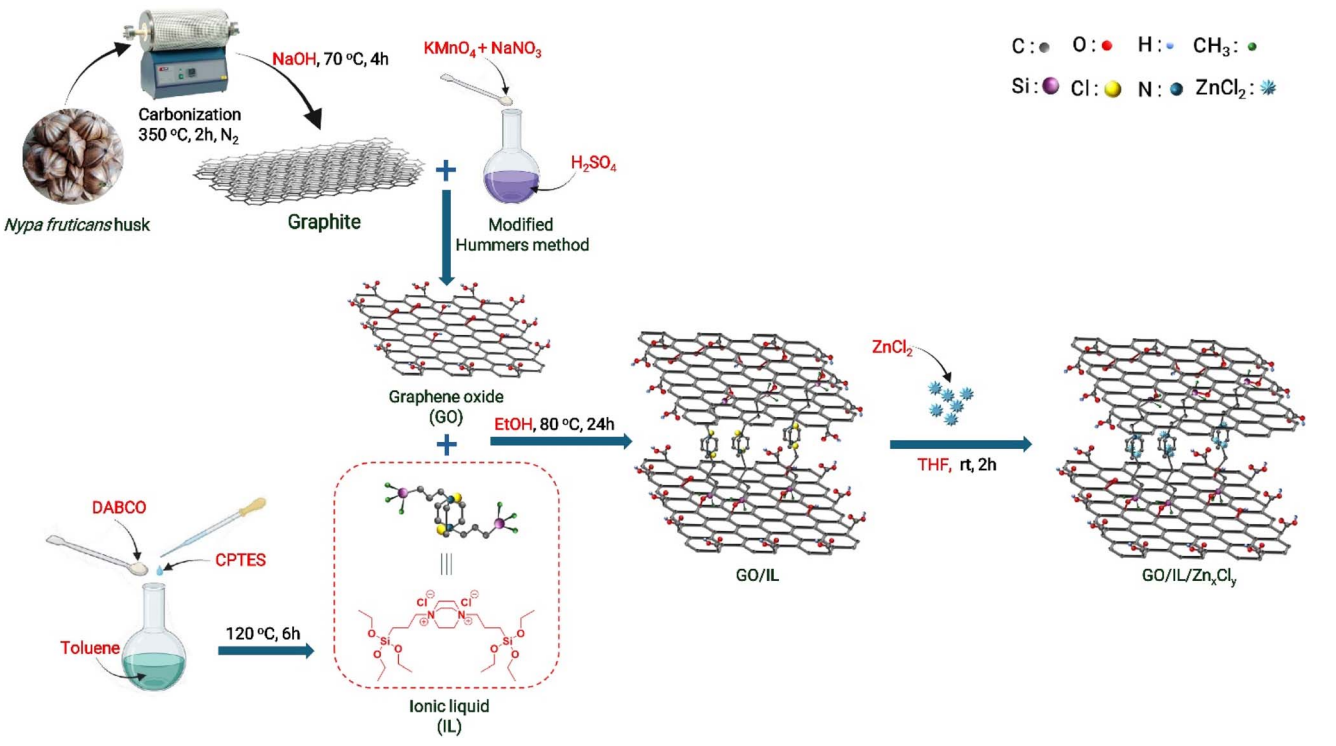

Scheme 1 Preparation process of GO/IL/Zn_xCl_y material from *Nypa fruticans* husk.

containing functional groups, enhancing further modifications. Next, GO was functionalized with an ionic liquid (IL), synthesized from DABCO and CPTES in the presence of toluene at 120 °C for 6 hours, ensuring proper functionalization. The IL modification step was performed in the presence of ethanol at 80 °C for 24 hours, allowing efficient interaction between IL and GO, leading to the formation of GO/IL. Finally, $ZnCl_2$ was added in the presence of tetrahydrofuran (THF) at room temperature (r.t.) for 2 hours, forming the GO/IL/Zn_xCl_y composite. This step enables zinc coordination, improving the structural and chemical properties of the GO/IL/Zn_xCl_y material. This well-optimized process results in a highly functionalized graphene-based composite, making it suitable for applications in catalysis. A comprehensive analysis of the GO/IL/Zn_xCl_y material's structure and surface properties was conducted using multiple characterization techniques such as FT-IR spectroscopy, Raman spectroscopy, X-ray diffraction (XRD), ICP-MS, SEM, EDX and, TGA.

The FT-IR spectra presented in Fig. 1 provide a comprehensive comparison of the component materials, including graphite, graphene oxide (GO), ionic liquid (IL), GO/IL, and GO/IL/Zn_xCl_y. The observed variations in peak intensities and shifts reveal key structural and chemical modifications occurring at different stages of material preparation. Upon the oxidation of graphite to graphene oxide (GO), the FT-IR spectrum consistently reveals the characteristic signals of oxygen-containing functional groups. Specifically, absorption bands corresponding to the stretching vibrations of hydroxyl (–OH) at 3400 cm^{-1}, carbonyl (C=O) at 1720 cm^{-1}, C=C at 1620 cm^{-1}, and epoxy (–C–O–C–) groups at 1220 cm^{-1} are observed on the GO surface.[32] When the ionic liquid (IL) is immobilized onto GO to form GO/IL, the FT-IR spectrum of this composite material exhibits a notable decrease in the intensity of the O–H peak. Concurrently, the emergence of new signals, including C–H stretching at 2900 cm^{-1}, N–C at 1500 cm^{-1}, and characteristic IL cationic vibrations in the fingerprint region (below 1200 cm^{-1}), serves as conclusive evidence for the successful immobilization of IL onto GO.[33] Furthermore, the interaction between GO/IL and $ZnCl_2$ is evidenced by a reduced shift in the O–H peak at 3400 cm^{-1}, indicating strong coordination between $ZnCl_2$ and the hydroxyl/carboxyl groups on GO/IL. Additionally, a new peak appears at 1000 cm^{-1}, corresponding to Si=O vibrations, suggesting the incorporation of silica species, potentially residual from precursors. Lastly, C–O–Si stretching vibrations are recorded at 900 cm^{-1}.[34]

X-ray diffraction (XRD) analysis is an essential tool for understanding the structural evolution of materials during chemical modifications (Fig. 2). The XRD pattern of pure graphite reveals two strong and sharp diffraction peaks at 2θ = 26.5° and 54.6°, corresponding to the (002) and (004) planes of hexagonal graphite, respectively.[30] The typical interlayer spacing (d-spacing) in graphite is approximately 3.35 Å, which aligns exceptionally well with previous studies on well-ordered crystalline graphite. Upon the oxidation of graphite to GO, the characteristic high-intensity peak at 26.5° undergoes significant attenuation, with the concomitant appearance of a broad diffraction peak positioned around 10.5°–11.5°. This shift indicates a substantial increase in interlayer spacing, typically expanding to around 7–8 Å due to the introduction of oxygen functional groups such as hydroxyl (–OH), epoxy (–C–O–C–), and carboxyl (–COOH) groups. The XRD pattern of GO/IL retains some characteristics of GO but also shows notable differences. The broad peak around 10°–12° remains, indicating the exfoliated structure of GO is preserved after ionic liquid (IL) functionalization. New diffraction peaks emerge at higher angles (30°–50°), suggesting that the incorporation of the ionic liquid (IL) may induce minor structural rearrangements. These novel peaks can be attributed to interactions between the IL cations

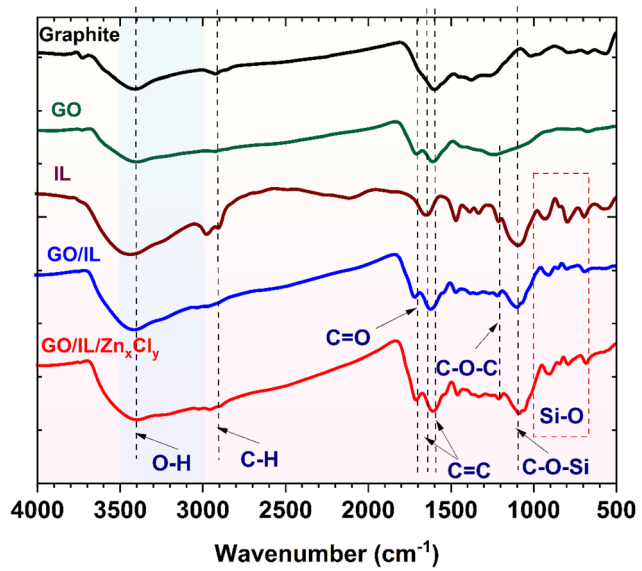

Fig. 1 FT-IR spectra of graphite, GO, IL, GO/IL, and GO/IL/Zn_xCl_y.

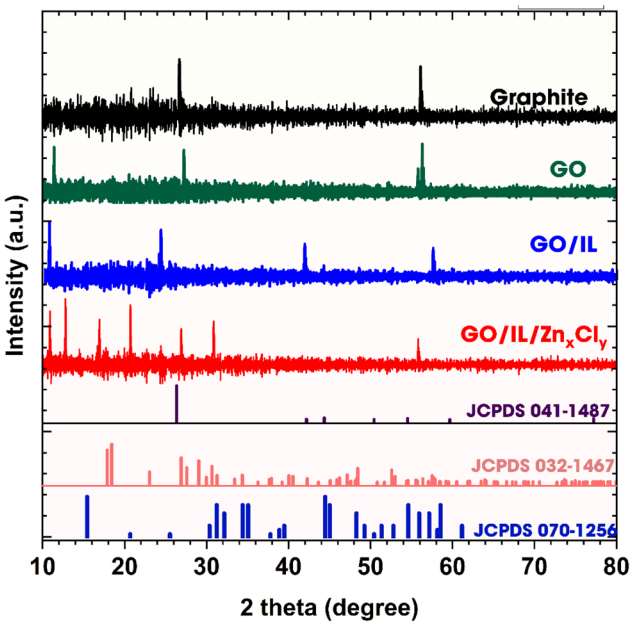

Fig. 2 XRD pattern of graphite, GO, IL, GO/IL, and GO/IL/Zn_xCl_y.

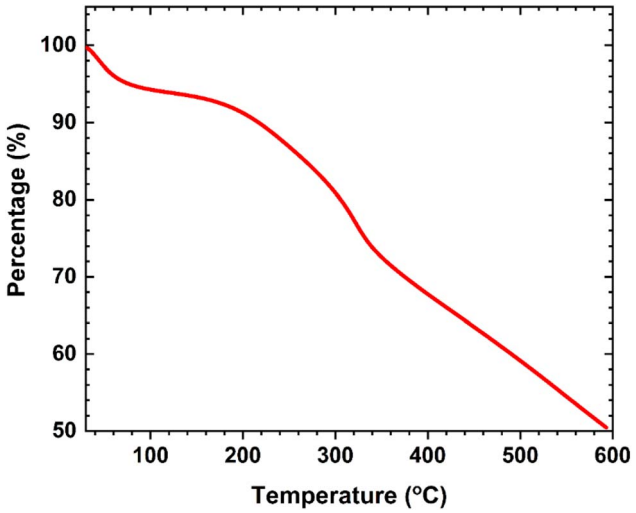

Fig. 3 TGA curve of GO/IL/Zn_xCl_y.

and the oxygen-functionalized GO sheets, potentially leading to a more ordered arrangement at the molecular level. Conversely, the XRD pattern of the GO/IL/Zn_xCl_y composite material exhibits multiple sharp and novel diffraction peaks in the 30°–50° range. This confirms the formation of new zinc-containing crystalline phases. Specifically, the observed peaks at 34.5° and 47.6° are consistent with the formation of $Zn(OH)_2$ or other zinc-containing hydroxyl compounds (JCPDS 041-1487). Peaks matching $ZnCl_2$ at 31.2°, 35.5°, and 56.7° (JCPDS no. 032-1467) indicate that unreacted or partially coordinated zinc chloride remains present within the material. Furthermore, the peaks at 31.7°, 34.5°, 36.2°, and 47.5° align with the characteristic reflections of ZnO (JCPDS no. 070-1256), suggesting that some zinc species have undergone hydrolysis or oxidation. The coexistence of $Zn(OH)_2$, $ZnCl_2$, and ZnO phases strongly implies that the zinc species have chemically interacted with GO, resulting in the formation of hybrid structures with complex mixed valency states within the GO/IL/Zn_xCl_y composite.

The thermogravimetric analysis (TGA) of GO/IL/Zn_xCl_y reveals its thermal stability and decomposition behavior through multiple weight loss stages (Fig. 3). Initially, a small weight loss occurs below 150 °C, attributed to the evaporation of physically adsorbed water and volatile components. As the temperature increases to the range of 150 °C to 300 °C, a gradual weight loss is observed, primarily due to the decomposition of the IL and the breakdown of oxygen-containing functional groups in GO. This stage highlights the thermal instability of IL and the partial reduction of GO. A major weight loss occurs between 300 °C and 500 °C, corresponding to the significant decomposition of GO and the $Zn_xCl_y^-$ complex. Additionally, the organic components in the material undergo carbonization, further contributing to mass loss. Beyond 500 °C, weight loss slows down, leaving a residual mass likely composed of thermally stable inorganic compounds, such as ZnO or other Zn-based structures. Overall, the TGA results indicate GO/IL/Zn_xCl_y exhibits moderate thermal stability, with substantial degradation occurring above 300 °C.

The SEM images provide a detailed visualization of the morphological evolution from pristine graphite to chemically modified GO composites, highlighting significant changes in structure, porosity, and surface characteristics at each stage (Fig. 4 and 5). Pristine graphite exhibits a highly ordered, compact, and crystalline layered structure. The SEM image reveals tightly stacked graphene layers with a relatively smooth surface and minimal defects. After oxidation, the morphology of graphite undergoes a drastic transformation. The SEM image reveals significant exfoliation, with GO sheets appearing rough, wrinkled, and porous, containing multiple circular voids. This structural disruption was attributed to the introduction of oxygen-containing functional groups, which disrupt the strong van der Waals interactions between graphene layers. The SEM image of GO/IL shows the material consists of smaller, more fragmented sheets compared to pure GO, suggesting that the

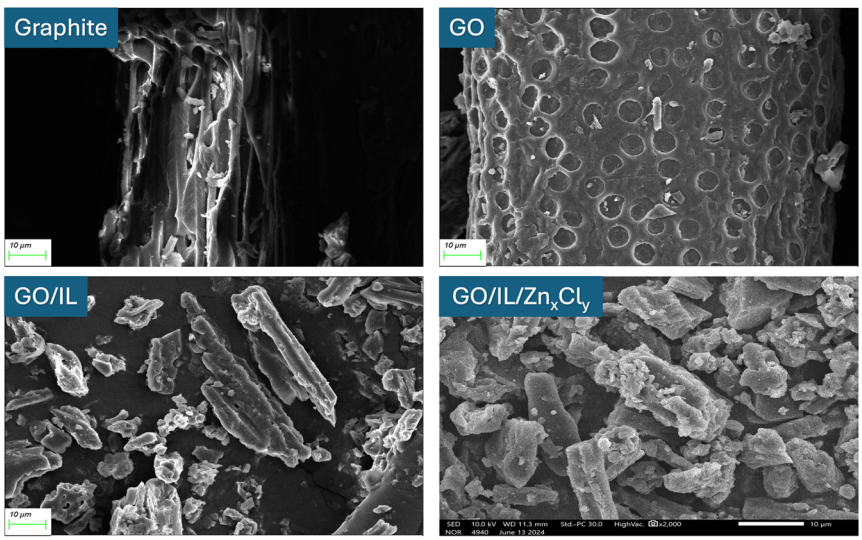

Fig. 4 SEM images of graphite, GO, GO/IL, and GO/IL/Zn_xCl_y.

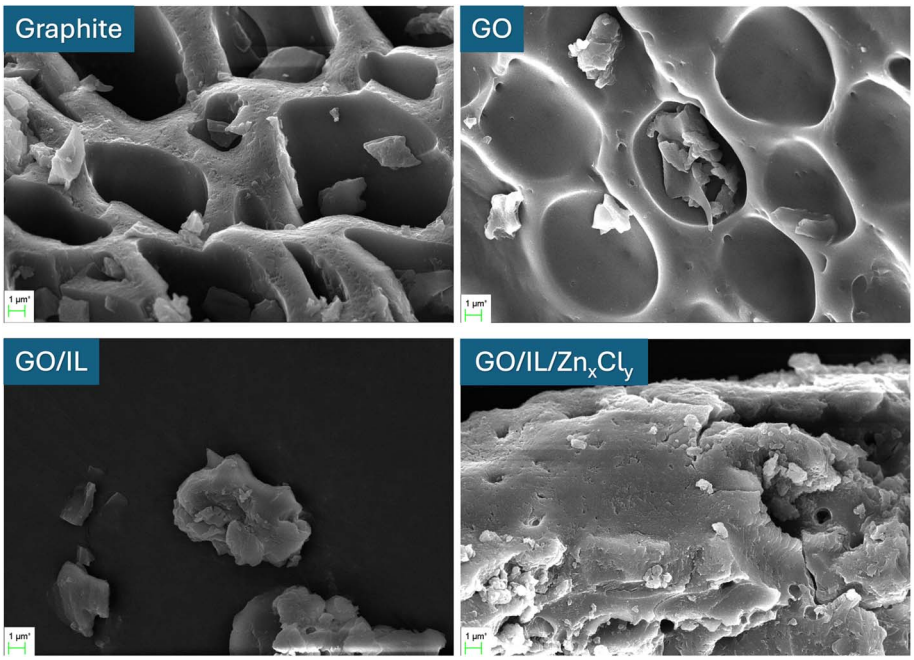

Fig. 5 FESEM images of graphite, GO, GO/IL, and GO/IL/Zn_xCl_y.

ionic liquid stabilizes the exfoliated graphene oxide layers and prevents reaggregation. The final modification stage, involving the introduction of $Zn_xCl_y^-$ into the GO/IL composite, results in even greater fragmentation and increased surface roughness. The SEM image demonstrates that the material consists of highly irregularly shaped flakes, with a rougher and more granular surface morphology than GO/IL.

Fig. 6 illustrates the particle size distribution of GO/IL/Zn_x-Cl_y, which appears right-skewed, suggesting that smaller particles are more prevalent while larger particles are less frequent. The peak frequency occurs around 10–15 μm, with a gradual decline in larger particle sizes beyond 30 μm. The overlaid curve follows a fitted probability density function.

The energy-dispersive X-ray spectroscopy (EDX) provides a comprehensive understanding of the elemental composition and structural evolution of the synthesized materials, including graphite, GO, GO/IL, and GO/IL/Zn_xCl_y (Fig. 7). Analysis of the intensity and position of characteristic peaks in the EDX results confirmed the successful functionalization and incorporation of various elements at each synthesis stage. The EDX spectrum of graphite, synthesized from *Nypa fruticans* husk, exhibited a strong and sharp carbon (C) peak at 0.27 keV. This confirms the high purity as a crystalline carbon material.[35] Oxidation of graphite into GO results in emergence of a significant oxygen

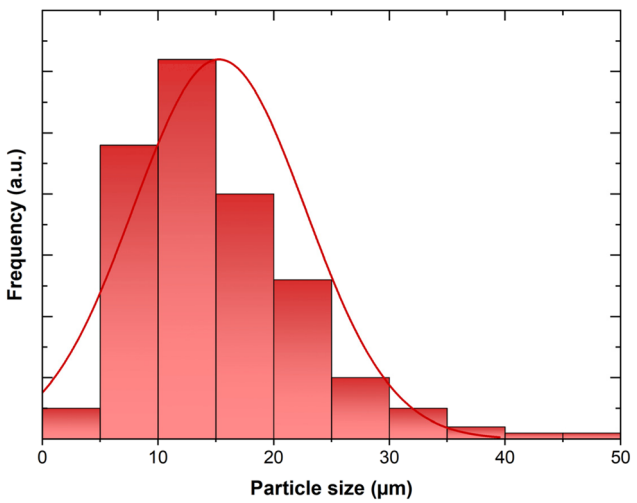

Fig. 6 Particle size distributions of GO/IL/Zn_xCl_y.

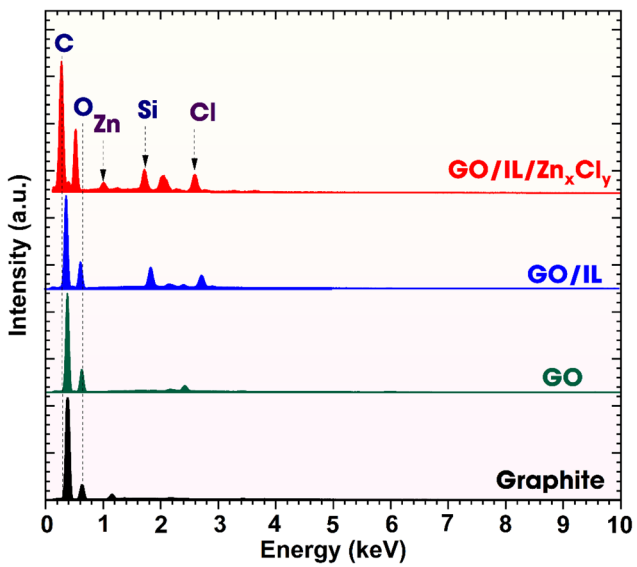

Fig. 7 EDS spectroscopy of graphite, GO, GO/IL, and GO/IL/Zn_xCl_y.

Table 1 EDS atomic percentages

	Element	Graphite	GO	GO/IL	GO/IL/Zn_xCl_y
Mass%	C	73.82	64.65	62.68	58.83
	N	0.00	2.89	5.77	3.50
	O	26.15	32.37	26.59	22.12
	Si	0.01	0.04	2.71	4.63
	Cl	0.01	0.06	2.25	8.46
	Zn	0.00	0.00	0.00	2.45
	Total	100.00	100.00	100.00	100.00
Atom%	C	78.98	70.68	70.02	70.26
	N	0.00	2.71	5.53	3.58
	O	21.01	26.57	22.30	19.83
	Si	0.01	0.02	1.30	2.37
	Cl	0.00	0.02	0.85	3.42
	Zn	0.00	0.00	0.00	0.54
	Total	100.00	100.00	100.00	100.00

(O) peak at 0.53 keV, confirming the formation of various oxygen-containing functional groups on the graphene sheets. The next stage involves the functionalization of GO with an ionic liquid (IL) to form the GO/IL composite. The GO/IL spectrum shows weak signals in the 1–3 keV range, indicating the presence of trace elements from the IL. The existence of oxygen groups also maintains the chemical activity of GO/IL, making it suitable for further modifications. Finally, the GO/IL/Zn_xCl_y spectrum displayed distinct peaks for zinc (Zn) and chlorine (Cl), confirming the successful incorporation of Zn-based compounds. Zinc (Zn) peaks appear at 1.01, 8.63, and 9.57 keV, corresponding to different Zn-based species or oxidation states, such as ZnO, $ZnCl_2$, or $Zn(OH)_2$. A strong chlorine (Cl) peak at 2.62 keV indicates the presence of chloride ions originating from $ZnCl_2$, suggesting possible ionic interactions between Zn^{2+} and Cl^- with GO/IL. A weak silicon (Si) peak at 1.74 keV is detected, attributed to from (3-chloropropyl)triethoxysilane during the preparation of IL.[36]

Table 1 shows the elemental composition analysis in both weight percentage (wt%) and atomic percentage (at%). From Table 1, carbon is the primary component of graphite (wt%: 73.82, at%: 83.02). The significant decrease in carbon percentage in GO (wt%: 64.65, at%: 77.23) indicates successful oxidation, where the introduction of oxygen-containing functional groups disrupted the highly ordered sp^2 carbon structure of graphite. Oxygen content is present in graphite (wt%: 26.15, at%: 16.78) due to minor surface oxidation. It significantly increases in GO (wt%: 32.37, at%: 21.08), confirming the successful formation of oxygen-rich functional groups. However, the oxygen percentage drops in GO/IL (wt%: 26.48, at%: 18.56), suggesting a partial reduction in oxygen content due to the formation of new interactions between IL molecules and the oxygen-containing groups. The most significant nitrogen increase is observed in GO/IL (wt%: 5.77, at%: 4.04), confirming the successful incorporation of nitrogen-rich IL molecules. Interestingly, nitrogen content decreases slightly in GO/IL/Zn_xCl_y (wt%: 3.50, at%: 2.78), implying partial nitrogen displacement by the $ZnCl_2$ modification. Silicon (Si) content increases from GO/IL (wt%: 2.71, at%: 1.95) to GO/IL/Zn_xCl_y (wt%: 4.63, at%: 3.03), suggesting silicon originated from impurities within the IL. Both chlorine (Cl) and zinc (Zn) contents significantly increase in GO/IL and GO/IL/Zn_xCl_y, confirming the influence of $ZnCl_2$ modification.

From Fig. 8, the EDX mapping confirmed the graphite consists primarily of carbon (C), with minimal traces of oxygen (O). In contrast, GO exhibits significantly higher oxygen content, which confirms the success of the oxidation process. The increased presence of O results from the formation of oxygen-containing functional groups (C–O, C═O, and COOH). Additionally, small traces of silicon (Si), chlorine (Cl), and nitrogen (N) are detected, indicating the successful incorporation of nitrogen-rich IL molecules into the GO structure. The uniform distribution of these elements suggests good interaction between GO and IL. The Zn distribution appears uniform, which indicates $ZnCl_2$ is coated onto the GO/IL.

The Raman spectrum is presented in Fig. 9, exhibiting characteristic peaks corresponding to different molecular vibrations. The peak around 500 cm^{-1} corresponds to Si–O bond vibrations, typical of silicate structures like silica (SiO_2). Additionally, a broad peak near 3400 cm^{-1} signifies O–H stretching vibrations, indicating the presence of hydroxyl groups or adsorbed water molecules. To quantify the disorder in the carbon structure, the I_D/I_G ratio was estimated. With the D and G band intensities of $I_D = 0.85$ and $I_G = 1.00$ respectively, the I_D/I_G ratio was determined to be 0.85. This value suggests a moderate level of disorder within the carbon structure, indicative of partially graphitized carbon. The correlation between the I_D/I_G ratio and disorder confirms the material's partial graphitization, as established by Ferrari & Robertson *et al.*[37] Furthermore, Dresselhaus *et al.* demonstrated that hydroxyl (–OH) functionalization is common in oxidized carbon materials, which is consistent with the broad OH band observed in this spectrum.[38]

2.2. Catalytic activity of GO/IL/Zn_xCl_y for 2-amino-3-cyanopyridine synthesis

In this work, GO/IL/Zn_xCl_y was employed as a novel catalyst to enhance reaction efficiency and yield under mild conditions. The combination of graphene oxide (GO), ionic liquid (IL), and zinc chloride-based catalytic systems ($ZnCl_2$) provides a unique hybrid material with improved catalytic performance, recyclability, and sustainability. Utilizing GO/IL/Zn_xCl_y as a catalyst, the study aims to develop a green chemistry approach that reduces energy consumption and minimizes waste. The reaction illustrates a multi-component approach for the synthesis of 2-amino-3-cyanopyridine derivatives from acetophenone (**1a**), benzaldehyde (**2a**), ammonium acetate (**3**), and malononitrile (**4**) (Scheme 2).

The experimental data highlights how intricate variations in reaction parameters can drastically affect the isolated yield of the reaction (Table S1). Temperature is shown to be a key determinant in driving the reaction forward. At room temperature (r.t.), the reaction yield was completely absent (0%, entry 1, Table S1), indicating that sufficient thermal energy is essential to overcome the activation energy barrier. As the

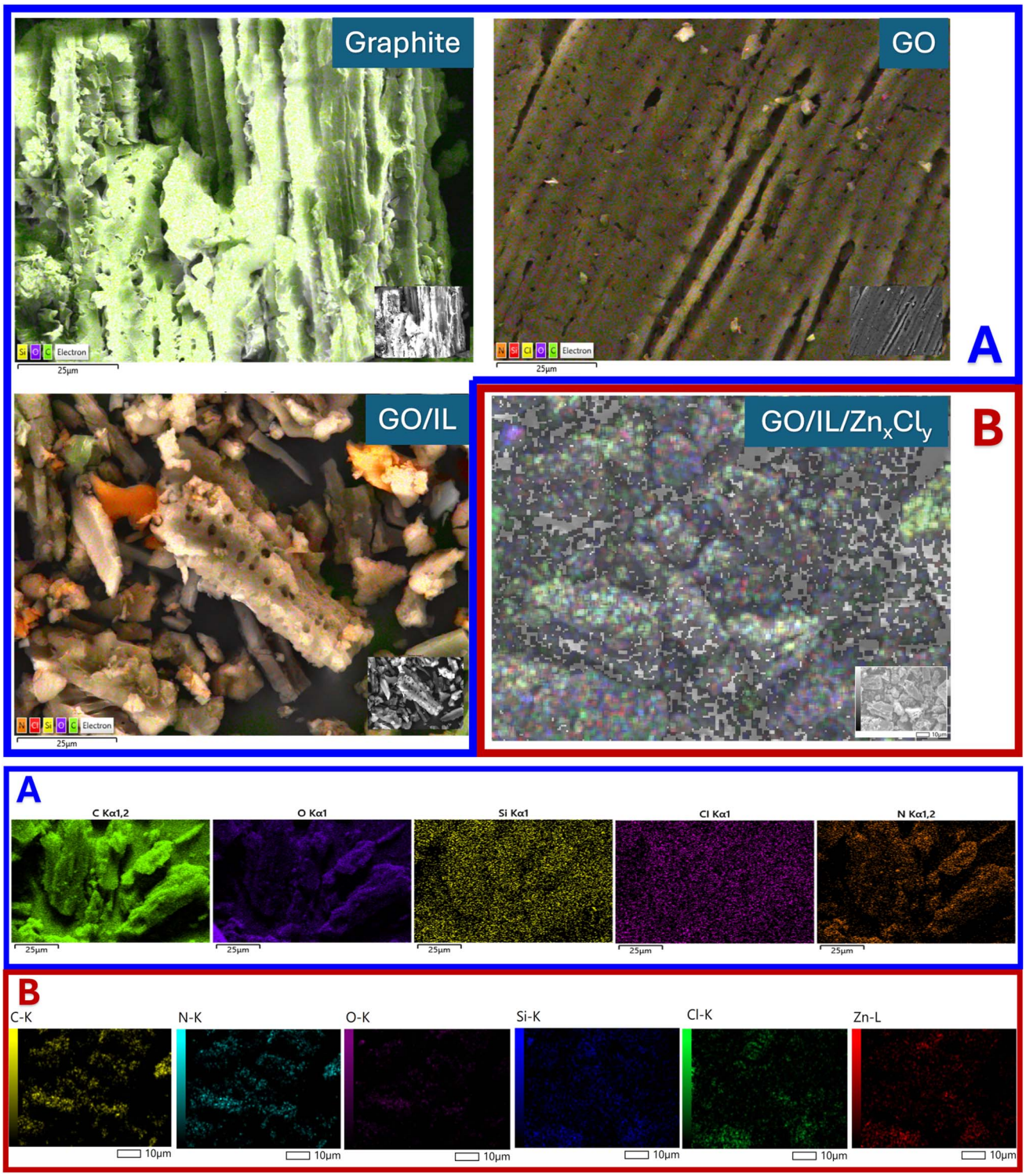

Fig. 8 EDS mapping of graphite, GO, GO/IL, and GO/IL/Zn_xCl_y.

temperature increased, the yield progressively increased, with notable enhancements observed at 70 °C (23%) and 90 °C (34%) (entries 3 and 4, Table S1). The optimal temperature was determined to be 110 °C, where a yield of 53% was achieved (entry 5, Table S1). However, raising the temperature to 130 °C resulted in a decrease in yield to 47% (entry 6, Table S1). This decline could be attributed to the thermal degradation of reactants or products or potential loss of catalytic activity at elevated temperatures. These results emphasize the need for a balanced temperature that provides sufficient energy for reaction progress without destabilizing the system. At 110 °C, shorter reaction times (5–30 minutes) produce yields ranging

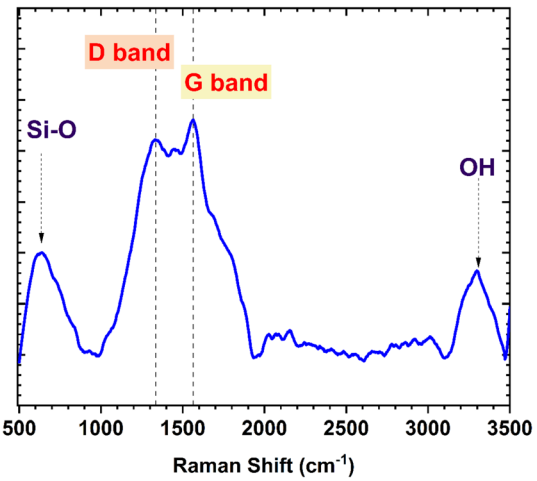

Fig. 9 Raman spectroscopy of GO/IL/Zn_xCl_y.

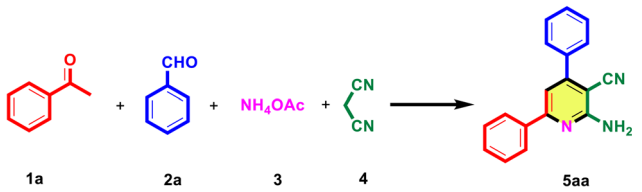

Scheme 2 Synthesis of 2-amino-3-cyano-4,6-diphenylpyridine (**5aa**).

from 42%–47% (entries 7–13, Table S1), likely due to incomplete conversion of reactants. The maximum yield of 53–57% was observed within the time range of 40–50 minutes (entries 5, 14 and 15, Table S1), indicating the optimal reaction duration. Reaction times were prolonged to 55 or 60 minutes led to a decline in yield, resulting in 43% (entry 16, Table S1) or 37% (entry 17, Table S1), respectively. The dataset demonstrates the choice of solvent has a profound effect on the reaction. Solvent-free conditions yielded the best result of 53% (entry 5, Table S1), suggesting that the reaction system is inherently efficient without the addition of a solvent. Polar solvents, such as water (0%, entry 18, Table S1), ethanol (20%, entry 19, Table S1), and DMSO (12%, entry 23, Table S1), generally hinder the reaction due to their incompatibility with the catalyst. Non-polar solvents, such as toluene (52%, entry 24, Table S1), exhibited much better performance, and cyclohexane (33%, entry 25, Table S1) also performs moderately well. Other solvents, such as ethyl acetate (23%, entry 21, Table S1) and acetonitrile (6%, entry 22, Table S1), exhibited moderate to poor performance, likely due to their partial solubility or interference with the catalytic process. Among the tested catalysts, GO/IL/Zn_xCl_y demonstrated the highest yields (53–55%, entries 5 and 40, Table S1). GO component achieved a yield of 35% (entry 28, Table S1). IL component performed better than GO, achieving 48% (entry 30, Table S1), likely due to its ability to enhance reaction kinetics and provide a compatible reaction medium. $ZnCl_2$ component resulted in a yield of 43% (entry 31, Table S1). GO/IL/Zn_xCl_y exhibited enhanced catalytic performance, likely due to improved surface area, active site accessibility, and efficient reactant–catalyst interactions. In contrast, other metal chloride catalysts, such as $CuCl_2$ (26%, entry 32, Table S1) and $FeCl_3$ (38%, entry 33, Table S1), performed significantly worse. The amount of catalyst used directly affects the reaction yield. A low catalyst GO/IL/Zn_xCl_y loading of 1 mg provided only a 35% yield (entry 38, Table S1), indicating insufficient active sites for efficient catalysis. Increasing the load to 5 mg of GO/IL/Zn_xCl_y achieved an optimal yield of 53% (entry 5, Table S1). Further increasing the GO/IL/Zn_xCl_y catalyst to 7 mg slightly improved the yield to 55% (entry 40, Table S1). However, when using a GO/IL/Zn_xCl_y loading of 10 mg, the yield was reduced to 52% (entry 41, Table S1), possibly due to catalyst aggregation or overloading, potentially blocking active sites and reducing efficiency. The stoichiometric ratio of reactants plays a vital role in determining reaction balance and efficiency. The ratio of 1 : 1 : 1.5 : 1 achieved the best yield of 53% (entry 5, Table S1). A 1 : 1 : 1 : 1 ratio reduced the yield to 42% (entry 42, Table S1), likely due to insufficient amounts of one or more key reactants. A 1 : 1 : 2 : 1 ratio slightly improved the yield to 47% (entry 43, Table S1).

The chosen reaction conditions exhibited exceptional catalytic efficacy, enabling the production of the necessary products with yields varying from adequate to excellent. The comprehensive results, featuring specific substrates and their respective yields, are shown in Scheme 3, demonstrating the protocol's efficacy in attaining high efficiency in the synthesis of 2-amino-3-cyanopyridine derivatives. The results presented in Scheme 4 demonstrate a series of synthesized compounds, along with their reaction yields. The reaction proceeded with benzaldehyde, affording a yield of 57%. Benzaldehyde derivatives played a pivotal role in modulating the yields. These substituents primarily affect the electronic properties of the aromatic ring, influencing the stability of the reaction intermediates and transition states. Halogens such as fluorine (–F) and chlorine (–Cl) are electron-withdrawing groups (EWGs), which resulted in moderate to low yields. For compounds **5ab** and **5bb**, with one and two-F groups on the *para* position of aromatic ring, respectively, significantly lower yield 40% and 23% were observed. The cumulative electron-withdrawing effect of the –F groups likely reduce the reactivity of the system, destabilizing intermediates. Benzaldehyde derivatives with electron-donating groups (EDGs) on the aromatic ring generally show higher yields. For instance, compound **5ae**, containing a methoxy (–OMe) group at the *para* position on the aromatic ring, achieved a good yield (54%). This can be explained by the methoxy group increasing the electron density on the ring, stabilizing the reaction intermediates and facilitating the formation of the desired product. Similarly, compound **5cc**, with a methyl (–Me) group on the aromatic ring at the *para* position, also exhibits a moderately high yield (48%). For instance, **5ca**, which contains a single –Me group on the aromatic ring, shows one of the lowest yields (22%). This suggests that in certain positions or electronic environments, even weakly electron-donating groups like –Me may hinder the reaction, possibly due to steric effects or unfavorable electronic interactions. The presence of a hydroxyl group (–OH) on the aromatic ring introduces

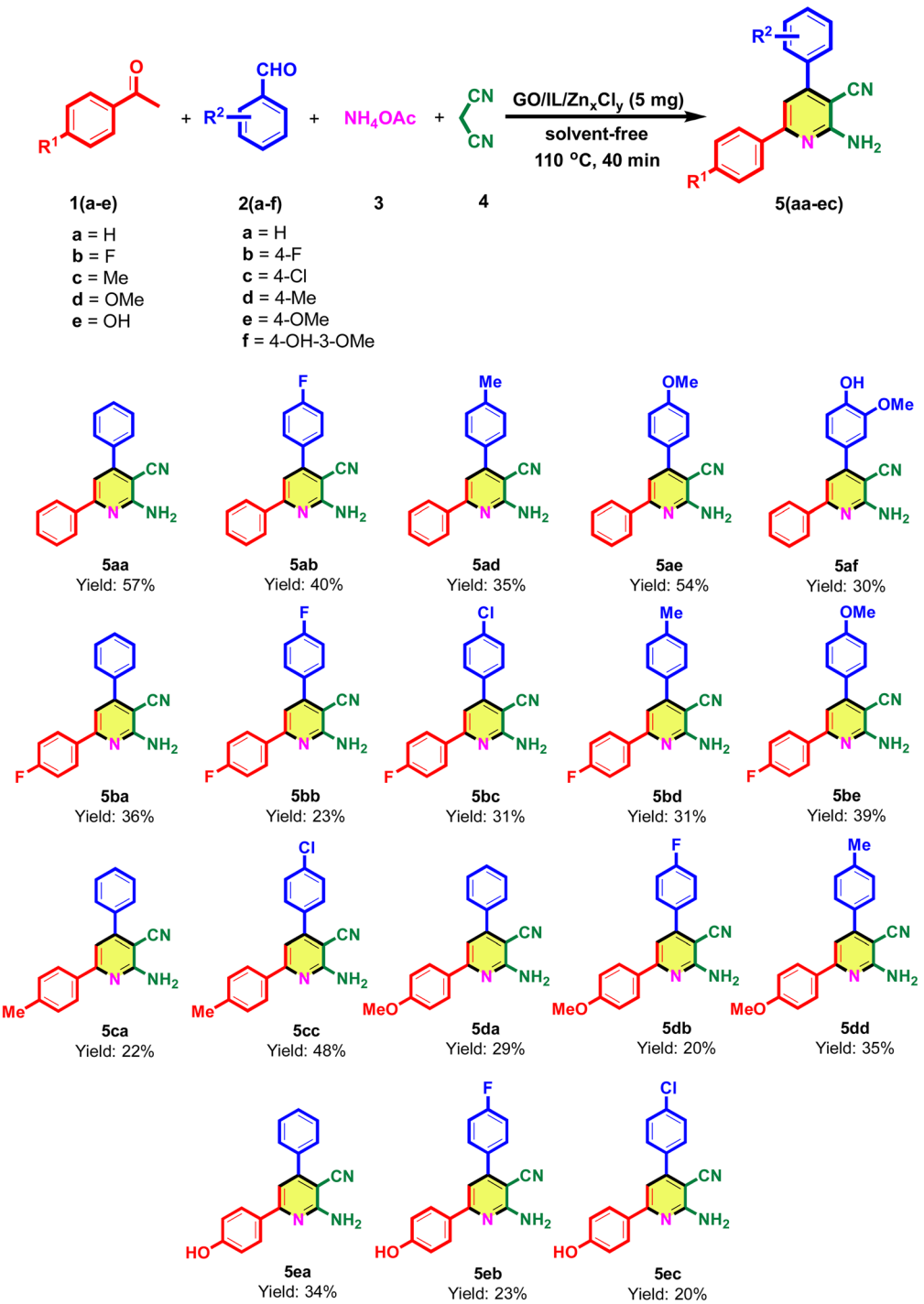

Scheme 3 Scope of 2-amino-3-cyanopyridine derivatives.[a] [a]Reaction conditions: arylaldehyde (1.0 mmol), acetophenones (1.0 mmol), ammonium acetate (1.5 mmol), malononitrile (1.0 mmol), GO/IL/Zn_xCl_y (5 mg), solvent-free, 110 °C, 40 min. Isolated yield by crystallization in ethanol (15–20 mL).

unique effects, as seen in **5ea** and **5eb**. The hydroxyl (–OH) group can act as both an electron donor (*via* resonance) and a hydrogen-bond donor, potentially stabilizing intermediates. **5ea**, with a single –OH group, achieves a moderate yield (34%), indicating a positive influence. However, when combined with a strong EWG like –F on the aromatic ring (**5eb**), the yield drops to 23%, suggesting an antagonistic interaction between the substituents. The aromatic ring, directly connected to the heterocyclic core, also plays a crucial role in determining yields. Substituents on this ring primarily influence the electron distribution and steric hindrance around the reactive sites. This demonstrates the importance of maintaining a balance between EDGs and EWGs on both rings. Compounds with substituents on both aromatic rings exhibited variable yields, depending on

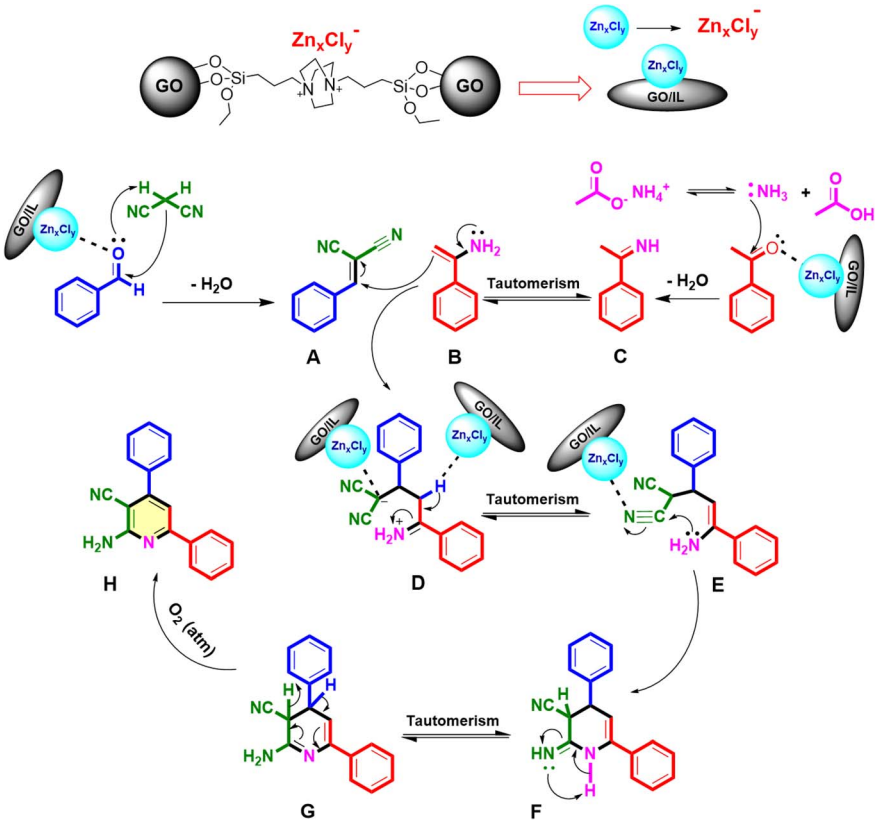

Scheme 4 Proposed reaction mechanism.

the interplay between their electronic and steric effects. Compound **5cc**, the *para*-substituted compound with a methyl group (–Me) and a chlorine (–Cl) on the respective aromatic rings, achieved a high yield (48%). The combination of an EDG and a moderately strong EWG likely balances electron distribution, creating favorable conditions for the reaction. In addition to electronic effects, steric hindrance played an important role in modulating yields. Bulky substituents could obstruct the approach of reactants to the reactive site, lowering yields. For example, compounds **5da** (29%) and **5db** (28%) both contain bulky methoxy (–OMe) groups, which are likely to introduce steric hindrance around the reaction center, reducing reaction efficiency. The combination of substituents on both rings can produce synergistic or antagonistic effects, emphasizing the importance of substituent compatibility.

2.3. The proposed mechanism of the 2-amino-3-cyanopyridine derivatives

Scheme 4 illustrates the reaction mechanism for the synthesis of 2-amino-3-cyanopyridine derivatives using GO/IL/Zn_xCl_y as a catalyst in the multi-step process. The presence of Zn^{2+} ions significantly improves catalytic activity by providing Lewis acidic sites, which facilitates the activation of reactants. The Zn-based catalyst effectively coordinates with both benzaldehyde and malononitrile, activating their functional groups and making them more reactive, thereby forming the intermediate (**A**). Malononitrile plays a crucial role as a key nucleophilic species in this reaction. The presence of Zn^{2+} ions increases its electrophilicity by stabilizing the negative charge during nucleophilic attacks. Meanwhile, acetophenone reacts with ammonium acetate, generating an intermediate enamine (**B**). The formation of this enamine is facilitated by the Zn catalyst, which stabilizes the transition state, thereby increasing the reaction rate in this Knoevenagel-related pathway. Next, the enamine intermediate (**B**) undergoes condensation with activated intermediate (**A**) in the presence of GO/IL/Zn_xCl_y. This Knoevenagel condensation resulted in the formation of a benzylidene-malononitrile derivative, which acts as a precursor to pyridine ring formation. The intermediate (**D**) undergoes an intramolecular cyclization facilitated by the GO/IL/Zn_xCl_y catalyst. The formation of the pyridine ring occurs through an electrophilic attack, leading to the closure of the six-membered heterocyclic system. This step is accompanied by proton transfers, which are stabilized by the presence of Zn^{2+} ions. Additionally, the catalyst helps to direct regioselectivity, ensuring the correct orientation of functional groups in the final product. In the final step, the newly formed 2-amino-3-cyanopyridine derivative undergoes structural stabilization. The involvement of GO/IL/Zn_xCl_y ensures high yield and selectivity, reducing unwanted byproducts. The catalytic system promotes aromatization, enhancing the stability of the pyridine ring and resulting in the formation of the desired heterocyclic compound.[39]

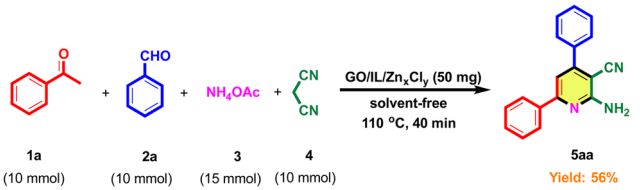

Scheme 5 Examination of scale-up in the **5aa** production process employing the GO/IL/Zn_xCl_y catalyst.

2.4. Synthesis of 5aa on a large-scale

Following Scheme 5, the optimal conditions were applied to scale up the multi-component reaction for the synthesis of 2-amino-3-cyano-4,6-diphenylpyridine (**5aa**) from acetophenone (**1a**) (10 mmol), benzaldehyde (**2a**) (10 mmol), ammonium acetate (**3**) (15 mmol), and malononitrile (**4**) (10 mmol). The reaction was carried out at 110 °C for 40 minutes under solvent-free conditions, affording a good yield of 56% with no significant loss in conversion.

2.5. Leaching test

The experimental results highlight the significant impact of the GO/IL/Zn_xCl_y catalyst on the synthesis yield of the target product under controlled conditions (110 °C, 20 minutes) (Scheme 6). In part I, the reaction was complete and the GO/IL/Zn_xCl_y catalyst was removed from the reaction mixture, resulting in a low yield of 26%. In part II, the GO/IL/Zn_xCl_y catalyst was removed before the reaction proceeding for an additional 20 minutes, leading to a slightly improved yield of 33%. In part III, the catalyst remained present throughout the entire reaction, the yield of 51% was achieved. The survey results demonstrate that GO/IL/Zn_xCl_y plays a crucial role in product formation and significantly enhances the reaction efficiency.

2.6. Assessment of green metrics

In recent years, the shift towards sustainable and environmentally friendly methods in organic synthesis has gained substantial momentum. Green chemistry has become a key pillar in evaluating chemical processes, aiming to reduce hazardous waste and optimize resource utilization. A particularly promising development in this area is the application of GO/IL/Zn_xCl_y as a catalyst in the synthesis of 2-amino-3-cyanopyridine frameworks. The environmental-factor (E-factor) of 1.40 indicates minimal waste production compared to traditional chemical synthesis, which often results in excessive by-products.[40] This stark reduction in waste underscores the efficiency of GO/IL/Zn_xCl_y as a catalyst. The atom economy (AE) was 73.44%, which reflects the substantial incorporation of reactant atoms into the final product. However, a more refined metric, actual atom efficiency (AEf), remained at 41.86%. While this demonstrates an improved utilization rate, some atoms were still lost in the process. Comparison to classical synthetic methods, which exhibit AEf values below 30%, represents a notable improvement. Process mass intensity (PMI) value of 2.40 indicates an efficient use of raw materials, minimizing excess reagent consumption. Compared to conventional reactions with PMI values exceeding 10, this method significantly reduces material waste.[41] However, the carbon efficiency (CE) of 51.3% suggests that half of the carbon atoms are not efficiently integrated into the target compound. The reaction mass efficiency (RME) was 41.63%, which reflects a moderate correlation between product yield and total reactant mass. Comparison with traditional organic syntheses, where RME values can be as low as 20%, this represents a significant step forward.[42] The eco-score of 58.5% positions this method among the more environmentally friendly synthesis methods available. Comparison with older methodologies that lack catalyst efficiency and resource optimization, this technique demonstrates clear advantages. However, ongoing research and further refinements in the atom economy, carbon efficiency, and reaction mass efficiency could push this process even closer to achieving the ideals of green chemistry.[43–46] (The calculated data is given in the SI).

2.7. The reusability of the GO/IL/Zn_xCl_y catalyst in the synthesis of 5aa

Recycling catalysts play a crucial role in eco-friendly chemical processes. In this investigation, the GO/IL/Zn_xCl_y catalyst underwent a systematic recovery process to determine its

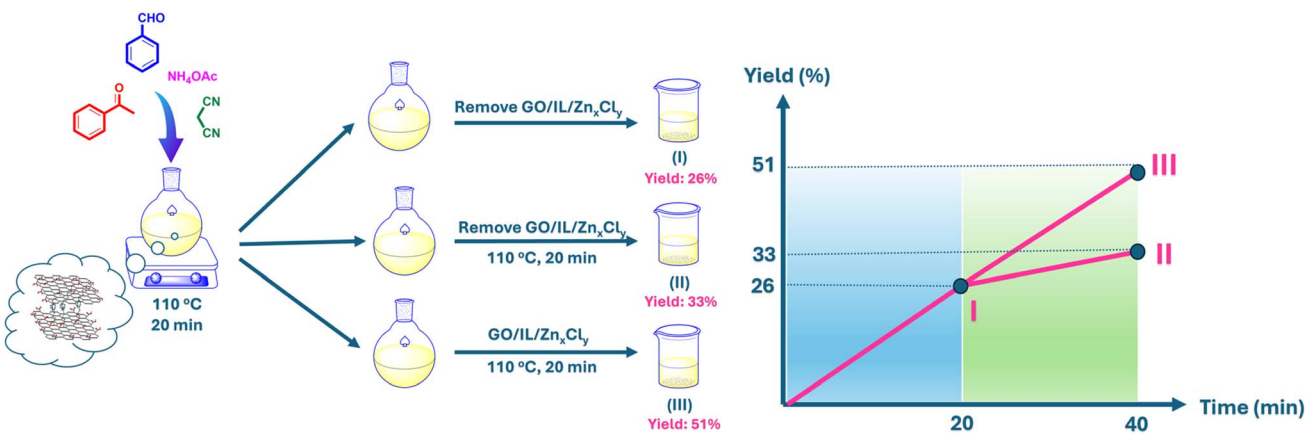

Scheme 6 Leaching test procedure: (I) reaction stopped; (II) reaction without GO/IL/Zn_xCl_y; (III) continuous reaction with GO/IL/Zn_xCl_y.

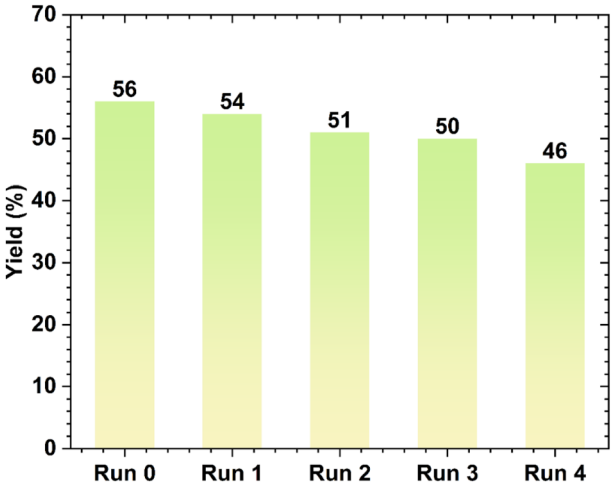

Fig. 10 Reusability of GO/IL/Zn_xCl_y for synthesis of **5aa**.

potential for reuse. After each reaction, the catalyst was separated through filtration, thoroughly rinsed with acetone to eliminate residual substances, and then left to dry before being reintroduced into further reactions. Fig. 10 illustrates the changes in catalytic efficiency over four reaction cycles. This decreasing trend indicates potential factors such as structural degradation, accumulation of impurities, or depletion of active catalytic sites, all of which contribute to the loss of efficiency. These factors include structural changes and loss of catalyst during the recovery and reuse process, which lead to a decrease in catalytic activity. Despite the observed decrease in efficiency, the catalyst still retains a relatively high yield of 46% after four reuses.

The characterization of the GO/IL/Zn_xCl_y catalyst before and after recovery revealed notable structural and compositional changes that affected its performance. The FT-IR spectra of the fresh and recovered GO/IL/Zn_xCl_y catalyst reveal noticeable structural changes after multiple catalytic cycles (Fig. S1). The new peaks corresponding to Si–O and C–O–Si bonds emerge in the recovered catalyst, which may result from contamination or interactions with reaction components over repeated cycles. The spectral changes suggest the GO/IL/Zn_xCl_y catalyst undergoes structural modifications during use. The loss or transformation of functional groups, coupled with potential contamination, may explain the observed decrease in catalytic activity over successive reaction cycles. SEM images show that the fresh catalyst possesses a uniform, layered morphology, while the recovered sample exhibits aggregated and irregular particles, indicating partial structural degradation. Particle size distribution shifts toward larger sizes after recovery, suggesting particle agglomeration, which may reduce catalytic efficiency (Fig. S2). XRD analysis confirms a loss of structural order, with decreased intensity of the (001) peak and reduced crystallinity, implying partial exfoliation and redistribution or leaching of $Zn_xCl_y^-$ species. Despite these changes, some Zn-containing crystalline phases remain (Fig. S3). EDS data further reveal an increase in carbon, nitrogen, and oxygen content, likely due to the removal of Zn and Cl and slight oxidation during the recovery process. The reduction in Zn and Cl content points to a partial loss of active catalytic species (Fig. S4). Elemental mapping shows Zn and Cl are less uniformly distributed post-recovery, while the GO structure appears more distinct and restored. These findings suggest that while the catalyst undergoes morphological and compositional degradation after repeated use, it still retains part of its original structure and functionality, making it potentially reusable with reduced, but not lost, catalytic activity (Fig. S5).

3. Experimental

3.1. Synthesis of GO/IL/Zn_xCl_y

3.1.1. Synthesis of graphite. *Nypa fruticans* husk was obtained from Cai Be District, Tien Giang Province, Vietnam. The raw material was washed and sun-dried for 3 days. Dried *Nypa fruticans* husk was then cut into small pieces and oven-dried at 100 °C for 6 hours to completely remove water and moisture. *Nypa fruticans* husk was carbonized at 350 °C in an N_2 atmosphere for 2 hours. Then, the sample was washed with sodium hydroxide (NaOH 2 M) to remove impurities and stirred at a sample-to-base ratio of 1 : 10 at 70 °C for 4 hours. The sample was washed with distilled water until it reached pH 7 and was dried in an oven at 100 °C for 8 hours.[47]

3.1.2. Synthesis of graphene oxide (GO). Modified Hummers' method was employed for synthesis of GO from *Nypa fruticans* husk.[47] 1.5 g of *Nypa fruticans* husk-derived activated charcoal was mixed with 0.75 g sodium nitrate ($NaNO_3$) and 34.5 mL of sulfuric acid (H_2SO_4 95%). The reaction mixture was stirred for 20 minutes and cooled to 0 °C. 4.5 g of $KMnO_4$ was added slowly in portions to maintain the reaction temperature below 20 °C. The sample was warmed to 35 °C and stirred for 30 minutes. Then, 69 mL of distilled water was added slowly over 20 minutes, maintaining the temperature below 50 °C. 100 mL of distilled water and 0.5 mL of 30% H_2O_2 were added to terminate the oxidation process. The mixture was sonicated for 2 hours and then allowed to settle for 24 hours to facilitate solid–liquid separation. The sample was washed with distilled water until neutral pH was achieved and dried in an oven at 100 °C for 12 hours to give 1.35 g of GO.

3.1.3. Synthesis of bis(*n*-propyltrimethoxysilane)-1,4-diazoniabicycle[2.2.2]octane chloride ionic liquid (IL). The mixture of DABCO (1 mmol) and (3-chloropropyl)triethoxysilane (2 mmol) in 10 mL toluene was stirred for 6 hours at 110 °C. After the reaction, the mixture was filtered and washed with diethyl ether several times. The white solid was desiccated and used for the next steps.[48]

3.1.4. Synthesis of graphene oxide modified by ionic liquids (GO/IL). GO modified by ionic liquids was prepared according to the procedure described by Jie Xu *et al.*[49] 1.0 g GO and 2.0 g of IL were transferred to a 100 mL flask, followed by the addition of 50 mL ethanol. The sample was sonicated three times, with each sonication lasting for 30 minutes. The mixture was then refluxed for 24 hours at 80 °C. Upon completion of the reaction, the sample was washed with ethanol several times. Finally, the solid was dried at 80 °C for 12 hours.

3.1.5. Synthesis of GO/IL/Zn_xCl_y. GO/IL/Zn_xCl_y was prepared according to the procedure described by Sadegh Rostamnia *et al.*[50] The mixture of 1 g GO/IL with 15 mL THF was stirred at room temperature for 30 minutes. Then, 80 mg $ZnCl_2$ was added to the mixture and stirred for 2 hours. After the reaction, the sample was washed with ethanol several times. The mixture was dried at 80 °C for 5 hours to obtain the final catalyst.

3.2. Application of GO/IL/Zn_xCl_y catalyst for one-pot synthesis of 2-amino-3-cyanopyridine derivatives

In a 5 mL COD tube, the mixture of arylaldehyde (1.0 mmol), acetophenone derivatives (1.0 mmol), ammonium acetate (1.5 mmol), and malononitrile (1.0 mmol) along with GO/IL/Zn_xCl_y catalyst (5.0 mg) was stirred for 40 minutes at 110 °C under solvent-free conditions. The progress of the reaction was observed using thin-layer chromatography (TLC) with a mixture of *n*-hexane and ethyl acetate (20%, v/v). After the completion of the reaction, the reaction mixture was allowed to cool to room temperature. Subsequently, 10 mL of ethanol was added, and the desired product was separated by filtration. The GO/IL/Zn_xCl_y catalyst was separated from the mixture by filtration. The catalyst was washed with acetone (5 mL × 5). Finally, the pure product was obtained by recrystallization from ethanol (15–20 mL) and washed with cold ethanol (3 mL × 5). The product's structure and purity were determined using ^{1}H-NMR and ^{13}C-NMR spectroscopy.

3.2.1. 2-Amino-3-cyano-4,6-diphenylpyridine (5aa). A yellow solid was obtained in 57% yield (m = 153.7 mg). R_f = 0.65 (*n*-hexane : ethyl acetate, v/v = 4 : 1). Mp = 185–186 °C [lit. = 187–188 °C].[51] ^{1}H NMR (500 MHz, $CDCl_3$): δ = 8.02–8.00 (m, 2H), 7.65–7.63 (m, 2H), 7.55–7.50 (m, 3H), 7.49–7.46 (m, 3H), 7.21 (s, 1H), 5.38 (s, 2H) ppm. ^{13}C NMR (125 MHz, $CDCl_3$): δ = 160.4, 160.0, 155.3, 138.1, 137.1, 130.3, 130.0, 129.1, 128.9, 128.3, 127.5, 117.3, 111.4, 88.4 ppm. UV (λ_{max}, ethyl acetate): 254.5 nm. IR (KBr, 4000–500) ν_{max} (cm^{-1}): 3463, 3298, 3174, 3061, 2201, 1634, 1563, 1255.

3.2.2. 2-Amino-3-cyano-4-(4-fluorophenyl)-6-phenylpyridine (5ab). A pink solid was obtained in 50% yield (m = 145.1 mg). R_f = 0.45 (*n*-hexane : ethyl acetate, v/v = 4 : 1). Mp = 163–164 °C [lit. = 148–150 °C].[51] ^{1}H NMR (500 MHz, $CDCl_3$): δ = 8.01–7.99 (m, 2H), 7.64–7.61 (m, 2H), 7.50–7.46 (m, 3H), 7.22 (t, J = 8.5 Hz, 17.5 Hz, 2H), 7.17 (s, 1H), 5.39 (s, 2H) ppm. ^{13}C NMR (125 MHz, $CDCl_3$): δ = 163.8 (d, J = 250.0 Hz), 160.4, 160.1, 154.2, 138.0, 133.1 (d, J = 3.3 Hz), 130.4, 130.3 (d, J = 8.5 Hz), 129.0, 127.5, 117.2, 116.2 (d, J = 21.8 Hz), 111.3, 88.3 ppm. UV (λ_{max}, ethyl acetate): 255.5 nm. IR (KBr, 4000–500) ν_{max} (cm^{-1}): 3475, 3313, 3189, 3065, 2209, 1638, 1566, 1232.

3.2.3. 2-Amino-3-cyano-4-(*p*-tolyl)-6-phenylpyridine (5ad). A yellow solid was obtained in 35% yield (m = 99.8 mg). R_f = 0.60 (*n*-hexane : ethyl acetate, v/v = 4 : 1). Mp = 159–160 °C [lit. = 172–175 °C].[39] ^{1}H NMR (500 MHz, $CDCl_3$): δ = 8.01–7.98 (m, 2H), 7.55 (d, J = 8.0 Hz, 2H), 7.50–7.45 (m, 3H), 7.33 (d, J = 7.5 Hz, 2H), 7.20 (s, 1H), 5.36 (s, 2H), 2.44 (s, 3H) ppm. ^{13}C NMR (125 MHz, $CDCl_3$): δ = 160.4, 159.9, 155.3, 140.2, 138.2, 134.2, 130.3, 129.8, 128.9, 128.2, 127.5, 117.4, 111.3, 88.4, 21.5 ppm. UV (λ_{max}, ethyl acetate): 256.0 nm. IR (KBr, 4000–500) ν_{max} (cm^{-1}): 3407, 3294, 3170, 3046, 2922, 2205, 1626, 1566, 1258.

3.2.4. 2-Amino-3-cyano-4-(4-methoxyphenyl)-6-phenylpyridine (5ae). A yellow solid was obtained in 39% yield (m = 119.1 mg). R_f = 0.45 (*n*-hexane : ethyl acetate, v/v = 4 : 1). Mp = 177–178 °C [lit. = 174–176 °C].[51] ^{1}H NMR (500 MHz, $CDCl_3$): δ = 8.00–7.99 (m, 2H), 7.61 (d, J = 8.5 Hz, 2H), 7.48–7.47 (m, 3H), 7.19 (s, 1H), 7.04 (d, J = 9.0 Hz, 2H), 5.35 (s, 2H), 3.88 (s, 3H) ppm. ^{13}C NMR (125 MHz, $CDCl_3$): δ = 161.1, 160.5, 159.8, 154.9, 138.2, 130.2, 129.8, 129.3, 128.9, 127.4, 117.6, 114.5, 111.2, 88.1, 55.6 ppm. UV (λ_{max}, ethyl acetate): 258.0 nm. IR (KBr, 4000–500) ν_{max} (cm^{-1}): 3501, 3396, 3305, 3185, 2926, 2205, 1608, 1570, 1240.

3.2.5. 2-Amino-3-cyano-4-(4-hydroxy-3-methoxyphenyl)-6-phenylpyridine (5af). A yellow solid was obtained in 20% yield (m = 61.7 mg). R_f = 0.45 (*n*-hexane : ethyl acetate, v/v = 3 : 2). Mp = 188–190 °C. ^{1}H NMR (500 MHz, $CDCl_3$): δ = 9.57 (s, 1H), 8.113–8.11 (m, 2H), 7.51–7.46 (m, 3H), 7.26 (s, 2H), 7.15 (dd, J = 2.0 Hz, 8.0 Hz, 1H), 6.92 (d, J = 8.0 Hz), 6.89 (s, 2H), 3.86 (s, 3H) ppm. ^{13}C NMR (125 MHz, $CDCl_3$): δ = 161.1, 158.5, 155.0, 148.3, 147.7, 137.8, 130.1, 128.7, 127.8, 127.3, 121.5, 117.6, 115.6, 112.6, 109.1, 86.5, 55.8 ppm. UV (λ_{max}, ethyl acetate) 255.5 nm. IR (KBr, 4000–500) ν_{max} (cm^{-1}): 3493, 3396, 3309, 3189, 3001, 2933, 2209, 1630, 1577, 1514, 1273.

3.2.6. 2-Amino-3-cyano-6-(4-fluorophenyl)-4-phenylpyridine (5ba). A white solid was obtained in 54% yield (m = 155.5 mg). R_f = 0.45 (*n*-hexane : ethyl acetate, v/v = 4 : 1). Mp = 220–221 °C. ^{1}H NMR (500 MHz, $CDCl_3$): δ = 8.03–8.00 (m, 2H), 7.64–7.62 (m, 2H), 7.55–7.51 (m, 3H), 7.17–7.14 (m, 3H), 5.36 (s, 2H) ppm. ^{13}C NMR (125 MHz, $CDCl_3$): δ = 164.3 (d, J = 250.0 Hz), 160.3, 158.8, 155.4, 137.0 (d, J = 3.8 Hz), 134.2, 130.4, 129.5 (d, J = 8.9 Hz), 129.1, 128.3, 117.2, 116.0 (d, J = 21.8 Hz), 111.0, 88.4 ppm. UV (λ_{max}, ethyl acetate) 255.0 nm. IR (KBr, 4000–500) ν_{max} (cm^{-1}): 3463, 3317, 3197, 3069, 2204, 1634, 1563, 1225.

3.2.7. 2-Amino-3-cyano-4,6-bis(4-fluorophenyl)pyridine (5bb). A pale-yellow solid was obtained in 28% yield (m = 86.4 mg). R_f = 0.50 (*n*-hexane : ethyl acetate, v/v = 4 : 1). Mp = 214–216 °C. ^{1}H NMR (500 MHz, $CDCl_3$): δ = 8.02–7.99 (m, 2H), 7.63–7.61 (m, 2H), 7.24–7.20 (m, 2H), 7.18–7.14 (m, 2H), 7.12 (s, 1H), 5.36 (s, 2H) ppm. ^{13}C NMR (125 MHz, $CDCl_3$): δ = 164.4 (d, J = 250.0 Hz), 163.8 (d, J = 248.8 Hz), 160.3, 158.9, 154.3, 134.0 (d, J = 3.8 Hz), 133.0 (d, J = 3.8 Hz), 130.3 (d, J = 8.5 Hz), 129.5 (d, J = 8.6 Hz), 117.1, 116.3 (d, J = 21.8 Hz), 116.0 (d, J = 25.5 Hz), 110.9, 88.3 ppm. UV (λ_{max}, ethyl acetate): 254.5 nm. IR (KBr, 4000–500) ν_{max} (cm^{-1}): 3497, 3392, 3197, 3080, 2205, 1612, 1559, 1232.

3.2.8. 2-Amino-3-cyano-4-(4-chlorophenyl)-6-(4-fluorophenyl)pyridine (5bc). A yellow solid was obtained in 31% yield (m = 100.7 mg). R_f = 0.52 (*n*-hexane : ethyl acetate, v/v = 4 : 1). Mp = 202–204 °C. ^{1}H NMR (500 MHz, $CDCl_3$): δ = 8.02–7.99 (m, 2H), 7.57 (d, J = 8.5 Hz, 2H), 7.50 (d, J = 8.5 Hz, 2H), 7.16 (t, J = 9.0 Hz, 17.5 Hz, 2H), 7.12 (s, 1H), 5.38 (s, 2H) ppm. ^{13}C NMR (125 MHz, $CDCl_3$): δ = 164.4 (d, J = 250.0 Hz), 160.3, 159.0, 154.1, 136.4, 135.4, 134.0 (d, J = 2.1 Hz), 129.6, 129.5 (d, J = 8.5 Hz), 129.4, 117.0, 116.0 (d, J = 21.6 Hz), 110.7, 88.1 ppm. UV

(λ_{max}, ethyl acetate): 256.0 nm. IR (KBr, 4000–500) ν_{max} (cm^{-1}): 3478, 3342, 3215, 3069, 2209, 1638, 1559, 1225.

3.2.9. 2-Amino-3-cyano-6-(4-fluorophenyl)-4-(*p*-tolyl)pyridine (5bd). A pale-yellow solid was obtained in 34% yield (m = 103.6 mg). R_f = 0.55 (*n*-hexane : ethyl acetate, v/v = 4 : 1). Mp = 204–206 °C [lit. = 198–200 °C].[52] ^{1}H NMR (500 MHz, $CDCl_3$): δ = 8.02–7.99 (m, 2H), 7.54 (d, J = 8.0 Hz, 2H), 7.33 (d, J = 8.5 Hz, 2H), 7.17–7.14 (m, 3H), 5.33 (s, 2H), 2.44 (s, 3H) ppm. ^{13}C NMR (125 MHz, $CDCl_3$): δ = 164.3 (d, J = 250.0 Hz), 160.3, 158.7, 155.4, 140.3, 134.3 (d, J = 3.0 Hz), 134.1, 129.8, 129.4 (d, J = 8.5 Hz), 128.2, 117.4, 115.9 (d, J = 21.5 Hz), 110.9, 88.3, 21.5 ppm. UV (λ_{max}, ethyl acetate): 256.0 nm. IR (KBr, 4000–500) ν_{max} (cm^{-1}): 3493, 3317, 3197, 3039, 2922, 2205, 1612, 1578, 1225.

3.2.10. 2-Amino-3-cyano-6-(4-fluorophenyl)-4-(4-methoxyphenyl)pyridine (5be). A yellow solid was obtained in 31% yield (m = 97.9 mg). R_f = 0.43 (*n*-hexane : ethyl acetate, v/v = 4 : 1). Mp = 193–195 °C [lit. = 186–189 °C].[52] ^{1}H NMR (500 MHz, $CDCl_3$): δ = 8.02–7.99 (m, 2H), 7.60 (d, J = 9.0 Hz, 2H), 7.17–7.13 (m, 3H), 7.04 (d, J = 8.5 Hz, 2H), 5.33 (s, 2H) ppm. ^{13}C NMR (125 MHz, $CDCl_3$): δ = 162.2 (d, J = 262.5 Hz), 160.4, 158.7, 155.0, 134.3 (d, J = 3.3 Hz), 129.8, 129.4 (d, J = 8.5 Hz), 129.2, 117.5, 115.9 (d, J = 21.6 Hz), 114.6, 110.8, 88.1, 55.6 ppm. UV (λ_{max}, ethyl acetate): 257.0 nm. IR (KBr, 4000–500) ν_{max} (cm^{-1}): 3475, 3332, 3208, 3069, 2956, 2209, 1619, 1570, 1236.

3.2.11. 2-Amino-3-cyano-4-phenyl-6-(*p*-tolyl)pyridine (5ca). A white solid was obtained in 29% yield (m = 82.5 mg). R_f = 0.52 (*n*-hexane : ethyl acetate, v/v = 4 : 1). Mp = 181–183 °C [lit. = 166–168 °C].[39] ^{1}H NMR (500 MHz, $CDCl_3$): δ = 7.91 (d, J = 8.5 Hz, 2H), 7.64–7.62 (m, 2H), 7.54–7.50 (m, 3H), 7.28 (d, J = 6.0 Hz, 2H), 7.19 (s, 1H), 5.36 (s, 2H), 2.42 (s, 3H) ppm. ^{13}C NMR (125 MHz, $CDCl_3$): δ = 160.4, 159.9, 155.1, 140.7, 137.2, 135.3, 129.9, 129.7, 129.1, 128.3, 127.4, 117.4, 111.1, 88.1, 21.5 ppm. UV (λ_{max}, ethyl acetate): 255.5 nm. IR (KBr, 4000–500) ν_{max} (cm^{-1}): 3478, 3313, 3193, 3035, 2926, 2201, 1630, 1570, 1247.

3.2.12. 2-Amino-3-cyano-4-(4-chlorophenyl)-6-(*p*-tolyl)pyridine (5cc). A yellow solid was obtained in 22% yield (m = 70.3 mg). R_f = 0.55 (*n*-hexane : ethyl acetate, v/v = 4 : 1). Mp = 183–186 °C [lit. = 175–177 °C].[39] ^{1}H NMR (500 MHz, $CDCl_3$): δ = 7.90 (d, J = 8.5 Hz, 2H), 7.58–7.55 (m, 2H), 7.51–7.48 (m, 2H), 7.28 (d, J = 8.0 Hz, 2H), 7.14 (s, 1H), 5.37 (s, 2H), 2.42 (s, 3H) ppm. ^{13}C NMR (125 MHz, $CDCl_3$): δ = 160.4, 160.2, 153.9, 140.9, 136.2, 135.6, 135.1, 129.7, 129.7, 129.4, 127.4, 117.2, 110.8, 87.8, 21.5 ppm. UV (λ_{max}, ethyl acetate): 259.5 nm. IR (KBr, 4000–500) ν_{max} (cm^{-1}): 3478, 3305, 3182, 3035, 2917, 2209, 1608, 1578, 1247.

3.2.13. 2-Amino-3-cyano-6-(4-methoxyphenyl)-4-phenylpyridine (5da). A yellow solid was obtained in 36% yield (m = 106.9 mg). R_f = 0.33 (*n*-hexane : ethyl acetate, v/v = 4 : 1). Mp = 183–184 °C [lit. = 167–169 °C].[39] ^{1}H NMR (500 MHz, $CDCl_3$): δ = 8.00–7.97 (m, 2H), 7.64–7.62 (m, 2H), 7.54–7.50 (m, 3H), 7.15 (s, 1H), 6.99 (d, J = 9.0 Hz, 2H), 5.33 (s, 2H), 3.87 (s, 3H) ppm. ^{13}C NMR (125 MHz, $CDCl_3$): δ = 161.6, 160.4, 159.5, 155.1, 137.3, 130.5, 129.9, 129.0, 129.0, 128.3, 117.5, 114.3, 110.6, 87.6, 55.6 ppm. UV (λ_{max}, ethyl acetate): 255.0 nm. IR (KBr, 4000–500) ν_{max} (cm^{-1}): 3486, 3362, 3197, 3058, 2971, 2201, 1619, 1570, 1240.

3.2.14. 2-Amino-3-cyano-4-(4-fluorophenyl)-6-(4-methoxyphenyl)pyridine (5db). A white solid was obtained in 48% yield (m = 152.9 mg). R_f = 0.35 (*n*-hexane : ethyl acetate, v/v = 4 : 1). Mp = 192–193 °C. ^{1}H NMR (500 MHz, $CDCl_3$): δ = 7.98 (d, J = 9.0 Hz, 2H), 7.63–7.60 (m, 2H), 7.23–7.29 (m, 2H), 7.11 (s, 1H), 6.99 (d, J = 9.0 Hz, 2H), 5.33 (s, 2H), 3.87 (s, 3H) ppm. ^{13}C NMR (125 MHz, $CDCl_3$): δ = 163.8 (d, J = 250.0 Hz), 161.7, 160.3, 159.6, 153.9, 133.3 (d, J = 3.8 Hz), 130.4, 130.3 (d, J = 8.4 Hz), 129.0, 117.4, 116.3 (d, J = 21.4 Hz), 114.3, 110.4, 87.4, 55.6 ppm. UV (λ_{max}, ethyl acetate) 256.0 nm. IR (KBr, 4000–500) ν_{max} (cm^{-1}): 3486, 3377, 3185, 3080, 2926, 2201, 1608, 1551, 1243.

3.2.15. 2-Amino-3-cyano-6-(4-methoxyphenyl)-4-(*p*-tolyl) pyridine (5dd). A pale-yellow solid was obtained in 34% yield (m = 110.1 mg). R_f = 0.38 (*n*-hexane : ethyl acetate, v/v = 4 : 1). Mp = 137–139 °C. ^{1}H NMR (500 MHz, $CDCl_3$): δ = 7.98 (d, J = 9.0 Hz, 2H), 7.53 (d, J = 8.0 Hz, 2H), 7.32 (d, J = 8.0 Hz, 2H), 7.14 (s, 1H), 6.98 (d, J = 9.0 Hz, 2H), 5.31 (s, 2H), 3.87 (s, 3H), 2.44 (s, 3H) ppm. ^{13}C NMR (125 MHz, $CDCl_3$): δ = 161.5, 160.4, 159.4, 155.1, 140.1, 134.3, 130.6, 129.7, 129.0, 128.2, 117.7, 114.3, 110.5, 87.5, 55.6, 21.5 ppm. UV (λ_{max}, ethyl acetate): 279.5 nm. IR (KBr, 4000–500) ν_{max} (cm^{-1}): 3460, 3358, 3177, 3050, 2922, 2201, 1619, 1570, 1232.

3.2.16. 2-Amino-3-cyano-6-(4-hydroxyphenyl)-4-phenylpyridine (5ea). A yellow solid was obtained in 23% yield (m = 65.6 mg). R_f = 0.38 (*n*-hexane : ethyl acetate, v/v = 3 : 2). Mp = 237–239 °C [lit. = 233–235 °C].[51] ^{1}H NMR (500 MHz, $CDCl_3$): δ = 9.97 (s, 1H), 8.00 (d, J = 9.0 Hz, 2H), 7.66–7.64 (m, 2H), 7.56–7.51 (m, 3H), 7.16 (s, 1H), 6.87–6.84 (m, 4H) ppm. ^{13}C NMR (125 MHz, $CDCl_3$): δ = 160.9, 159.6, 158.7, 154.6, 137.3, 129.6, 129.1, 128.8, 128.4, 128.4, 117.4, 115.5, 108.3, 85.4 ppm. UV (λ_{max}, ethyl acetate): 256.0 nm. IR (KBr, 4000–500) ν_{max} (cm^{-1}): 3463, 3358, 3223, 3043, 2198, 1608, 1574, 1225.

3.2.17. 2-Amino-3-cyano-4-(4-fluorophenyl)-6-(4-hydroxyphenyl)pyridine (5eb). A yellow solid was obtained in 19% yield (m = 59.3 mg). R_f = 0.38 (*n*-hexane : ethyl acetate, v/v = 3 : 2). Mp = 257–259 °C. ^{1}H NMR (500 MHz, $CDCl_3$): δ = 9.98 (s, 1H), 8.01–7.98 (m, 2H), 7.73–7.69 (m, 2H), 7.40–7.36 (m, 2H), 7.15 (d, J = 6.5 Hz, 1H), 6.89–6.83 (m, 4H) ppm. ^{13}C NMR (125 MHz, $CDCl_3$): δ = 162.9 (d, J = 250.0 Hz), 160.8, 159.7, 158.8, 153.5, 133.7 (d, J = 3.8 Hz), 130.8 (d, J = 8.1 Hz), 129.1, 128.4, 117.4, 115.8 (d, J = 21.4 Hz), 115.5, 108.3, 85.3 ppm. UV (λ_{max}, ethyl acetate): 256.5 nm. IR (KBr, 4000–500) ν_{max} (cm^{-1}): 3470, 3362, 3144, 2209, 1608, 1566, 1232.

3.2.18. 2-Amino-3-cyano-4-(4-chlorophenyl)-6-(4-hydroxyphenyl)pyridine (5ec). A pale-yellow solid was obtained in 23% yield (m = 72.3 mg). R_f = 0.40 (*n*-hexane : ethyl acetate, v/v = 4 : 1). Mp = 276–278 °C [lit. = 270–272 °C].[51] ^{1}H NMR (500 MHz, $CDCl_3$): δ = 9.98 (s, 1H), 7.99 (d, J = 9.0 Hz, 2H), 7.69–7.66 (m, 2H), 7.62–7.60 (m, 2H), 7.16 (s, 1H), 6.91 (s, 2H), 6.85 (d, J = 8.5 Hz, 2H) ppm. ^{13}C NMR (125 MHz, $CDCl_3$): δ = 160.8, 159.7, 158.9, 153.3, 136.1, 134.5, 130.3, 129.1, 128.8, 128.3, 117.2, 115.5, 108.2, 85.2 ppm. UV (λ_{max}, ethyl acetate): 260.0 nm. IR (KBr, 4000–500) ν_{max} (cm^{-1}): 3467, 3347, 3234, 3077, 2205, 1619, 1566, 1236.

3.3. Leaching test procedures

To investigate catalytic stability under optimized reaction parameters, a leaching test was performed to confirm catalyst

activity. The experimental procedure was prepared, including benzaldehyde (3 mmol), acetophenone (3 mmol), malononitrile (3 mmol), ammonium acetate (4.5 mmol) in the presence of GO/IL/Zn_xCl_y (15 mg) under solvent-free conditions at 110 °C for 20 minutes. The reaction was examined through two distinct stages.

Stage 1: the initial reaction proceeded under optimal conditions for 20 minutes. Subsequently, the reaction mixture was divided into three portions for further investigation in the next stage. In the first portion, the reaction was terminated; after filtration and recrystallization, the product was obtained in the 26% yield.

Stage 2: the reaction was extended until the end of the 20 minute period. After filtration and removal of the catalyst, the reaction continued under optimal conditions for another 20 minutes, leading to a 33% yield of the desired product upon completion.

Stage 3: the reaction was maintained under optimal conditions for the entire 40 minute period. After filtration and removal of the catalyst, the product yielded 51% after recrystallization.

3.4. Large-scale

In addition, we investigated the general synthetic reaction on a 10 mmol scale while maintaining the optimal conditions. This experiment was conducted to evaluate the operational feasibility and application of our catalyst. The results show that the large-scale production of the desired product yielded a 56% efficiency, which is comparable to the results obtained from the small-scale experiment.

3.5. General procedure for the recycling of GO/IL/Zn_xCl_y

In a 5 mL COD tube, a mixture of 4-methoxybenzaldehyde (10 mmol), acetophenone (10 mmol), ammonium acetate (15 mmol), malononitrile (10 mmol), and GO/IL/Zn_xCl_y (50 mg) was stirred under solvent-free conditions at 110 °C. After cooling the reaction mixture, 25 mL of EtOH was added, the precipitate appeared on the COD tube. The precipitate and catalyst were washed several times with EtOH to completely remove undesired impurities. The solid was then dissolved in 30–35 mL of ethanol and heated until dissolution was complete. Hot filtration was performed to separate the insoluble catalyst, and the filtration was evaporated to yield the product. The recovered catalyst was washed several times with 15–20 mL of acetone and ethyl acetate to remove any residual product. The catalyst was then dried at 100 °C for 3 hours. The mass of the isolated product was 1.4910 g (56% yield). The mass of the catalyst recovered in the first run was 43.5 mg. This recovered catalyst (43.5 mg) was then used in subsequent recovery runs.

4. Conclusion

This study highlights the successful application of GO/IL/Zn_xCl_y as a novel and green catalyst for the synthesis of 2-amino-3-cyanopyridine derivatives. This study aims to develop an innovative synthesis approach for GO/IL/Zn_xCl_y using *Nypa fruticans* husk as a precursor. By integrating graphene oxide (GO), ionic liquid (IL), and zinc chloride-based catalytic systems ($Zn_xCl_y^-$), we developed a novel hybrid material with enhanced catalytic activity, improved selectivity, and superior recyclability. The catalyst's performance was systematically evaluated through a detailed investigation of its structural components. The combination of GO, IL, and Zn-based species provided synergistic effects, facilitating the activation of reactants, improving surface interactions, and enhancing overall catalytic performance. The recyclability and stability of GO/IL/Zn_xCl_y were also confirmed, further supporting its practical applicability in sustainable organic synthesis. Additionally, the solvent-free conditions not only improved the reaction yield but also reduced environmental impact by minimizing solvent waste, making this a promising green chemistry approach. The substrate scope study confirmed that the developed methodology is highly versatile, enabling the synthesis of a broad range of 2-amino-3-cyanopyridine derivatives with moderate to excellent yields. The optimization of reaction conditions-including temperature, reaction time, solvent selection, catalyst loading, and reactant ratio-demonstrated a significant impact on reaction efficiency and yield. The highest yield of 57% was achieved under optimal conditions (110 °C, 40 min, solvent-free), emphasizing the importance of carefully tuning reaction parameters to achieve maximum efficiency.

Author contributions

Y.-Nhi Thi Nguyen: investigation, methodology, resources, formal analysis, validation, data curation, and writing – original draft. Dat Minh Tran: investigation, methodology, resources, formal analysis, validation, data curation, and writing – original draft. The Thai Nguyen: validation, data curation, and writing – original draft. Hai Truong Nguyen: methodology, resources, formal analysis, validation, data curation, writing – review and editing, and supervision.

Conflicts of interest

The authors declare that they have no known competing financial interests or personal relationships that could have appeared to influence the work reported in this paper.

Data availability

The authors confirm that the data supporting the findings of this study are available within the article. Raw data that support the findings of this study are available from the corresponding author, upon reasonable request.

Supplementary information is available. See DOI: **https://doi.org/10.1039/d5ra04734j**.

Acknowledgements

This research is funded by Vietnam National University, Ho Chi Minh City (VNU-HCM) under grant number B2025-18-05.

References

1 A. Wiyono, N. W. Mohd Zulkifli, W. M. A. Wan Daud, Y. Sukrawan, R. Anggrainy, A. Syafrinaldy, H. Nolandy, A. Abidin, R. Sukarno and M. Aziz, *Energy Technol.*, 2024, **13**, 2401228.

2 S. Rana and S. B. Jonnalagadda, *Catal. Commun.*, 2017, **92**, 31–34.

3 S. Khabnadideh, E. Mirzaei and L. Amiri-Zirtol, *J. Mol. Struct.*, 2022, **1261**, 132934.

4 R. Ghafouri-Nejad, M. Hajjami and R. Nejat, *Appl. Organomet. Chem.*, 2018, **32**, e4248.

5 F. Dadvar and D. Elhamifar, *Nanoscale Adv.*, 2024, **6**, 5398–5408.

6 V. V. Gaikwad, V. B. Saptal, K. Harada, T. Sasaki, D. Nishio-Hamane and B. M. Bhanage, *ChemNanoMat*, 2018, **4**, 575–582.

7 S. W. Zhang, M. Zhang, F. Wang and H. Zeng, *Chem. Eng. J.*, 2022, **430**, 132619.

8 I. T. Kim, A. Magasinski, K. Jacob, G. Yushin and R. Tannenbaum, *Carbon*, 2013, **52**, 56–64.

9 L. Shen, W. Zhao and L. Miao, *J. Hazard. Mater.*, 2021, **403**, 123670.

10 W. Yu, L. Sisi, Y. Haiyan and L. Jie, *RSC Adv.*, 2020, **10**, 15328–15345.

11 P. Sharma, S. Sharma and H. Kumar, *J. Mol. Liq.*, 2024, **393**, 123447.

12 P. Coimbra, A. M. A. Dias and H. C. de Sousa, *Chem. Eng. J.*, 2025, **504**, 159039.

13 T. P. Mabate, N. P. Maqunga, S. Ntshibongo, M. Maumela and N. Bingwa, *SN Appl. Sci.*, 2023, **5**, 196.

14 H. R. Ahmed, A. O. B. Shekh, M. A. Salih, D. N. H. Saeed, A. M. Ealias and G. George, *J. Mol. Struct.*, 2025, **1331**, 141646.

15 S. Irfan, M. Aalim, M. H. Flaifel, I. Nazir, M. A. Shah, M. Q. Lone, A. Firdous, A. H. Pandith and G. N. Dar, *J. Energy Storage*, 2025, **106**, 114788.

16 S. Thakur, A. Ojha, S. K. Kansal, N. K. Gupta, H. C. Swart, J. Cho, A. Kuznetsov, S. Sun and J. Prakash, *Adv. Powder Mater.*, 2024, **3**, 100233.

17 M. Muschi and C. Serre, *Coord. Chem. Rev.*, 2019, **387**, 262–272.

18 K. Rana, H. Kaur, N. Singh, T. Sithole and S. S. Siwal, *Next Mater.*, 2024, **3**, 100107.

19 V. Georgakilas, J. N. Tiwari, K. C. Kemp, J. A. Perman, A. B. Bourlinos, K. S. Kim and R. Zboril, *Chem. Rev.*, 2016, **116**, 5464–5519.

20 J. Sahoo, C. R. Sahoo, P. K. N. Sarangi, S. K. Prusty, R. N. Padhy and S. K. Paidesetty, *Eur. J. Med. Chem.*, 2020, **186**, 111911.

21 S. Maračić, T. G. Kraljević, H. Č. Paljetak, M. Perić, M. Matijašić, D. Verbanac, M. Cetina and S. Raić-Malić, *Bioorg. Med. Chem.*, 2015, **23**, 7448–7463.

22 A. Al-Mulla, *Pharma Chem.*, 2017, **9**, 141–147.

23 R. Mishra, K. K. Jha, S. Kumar and I. Tomer, *Pharma Chem.*, 2011, **3**, 38–54.

24 K. Pluta, B. Morak-Młodawska and M. Jeleń, *Eur. J. Med. Chem.*, 2011, **46**, 3179–3189.

25 A. Mermer, T. Keles and Y. Sirin, *Bioorg. Chem.*, 2021, **114**, 105076.

26 C. B. Sangani, J. A. Makawana, X. Zhang, S. B. Teraiya, L. Lin and H.-L. Zhu, *Eur. J. Med. Chem.*, 2014, **76**, 549–557.

27 S. Liao, S. Shang, M. Shen, X. Rao, H. Si, J. Song and Z. Song, *Front. Agric. Sci. Eng.*, 2015, **2**, 335.

28 R. A. Zailaee, S. A. Zailaie, T. M. Sobahy, Z. M. Al-Amshany, K. O. Al-Footy and R. M. El-Shishtawy, *J. Mol. Struct.*, 2024, **1301**, 137309.

29 P. N. Kalaria, S. P. Satasia, J. R. Avalani and D. K. Raval, *Eur. J. Med. Chem.*, 2014, **83**, 655–664.

30 L. Xu, L. Shi, S. Qiu, S. Chen, M. Lin, Y. Xiang, C. Zhao, J. Zhu, L. Shen and Z. Zuo, *Drug Des., Dev. Ther.*, 2019, **13**, 3369–3381.

31 R. Sabour, M. F. Harras and A. B. M. Mehany, *Bioorg. Chem.*, 2020, **94**, 103358.

32 S. Kargar, D. Elhamifar and A. Zarnegaryan, *Surf. Interfaces*, 2021, **23**, 100946.

33 S. Momeni and R. Ghorbani-Vaghei, *Sci. Rep.*, 2024, **14**, 21531.

34 Q. Lyu, H. Yan, L. Li, Z. Chen, H. Yao and Y. Nie, *Polymers*, 2017, **9**, 447.

35 T.-H. Tran, R. D. Rodriguez, M. Salerno, A. Matković, C. Teichert and E. Sheremet, *Carbon*, 2021, **176**, 431–439.

36 S. Mahmud, *J. Alloys Compd.*, 2011, **509**, 4035–4040.

37 A. C. Ferrari and J. Robertson, *Phys. Rev. B: Condens. Matter Mater. Phys.*, 2000, **61**, 14095.

38 A. Jorio, M. S. Dresselhaus, R. Saito and G. Dresselhaus, *Raman Spectroscopy in Graphene Related Systems*, John Wiley & Sons, 2011.

39 R. Achagar, A. Elmakssoudi, A. Thoume, M. Dakir, A. Elamrani, Y. Zouheir, M. Zahouily, Z. Ait-Touchente, J. Jamaleddine and M. M. Chehimi, *Appl. Sci.*, 2022, **12**, 5487.

40 R. A. Sheldon, *Green Chem.*, 2023, **25**, 1704–1728.

41 E. R. Monteith, P. Mampuys, L. Summerton, J. H. Clark, B. U. W. Maes and C. R. McElroy, *Green Chem.*, 2020, **22**, 123–135.

42 A. P. Dicks and A. Hent, in *Green Chemistry Metrics: A Guide to Determining and Evaluating Process Greenness*, ed. A. P. Dicks and A. Hent, Springer International Publishing, Cham, 2015, pp. 17–44, DOI: 10.1007/978-3-319-10500-0_2.

43 R. A. Sheldon, *ACS Sustainable Chem. Eng.*, 2018, **6**, 32–48.

44 D. J. C. Constable, A. D. Curzons and V. L. Cunningham, *Green Chem.*, 2002, **4**, 521–527.

45 K. Van Aken, L. Strekowski and L. Patiny, *Beilstein J. Org. Chem.*, 2006, **2**, 3.

46 N. Sahiba, A. Sethiya, J. Soni and S. Agarwal, *ChemistrySelect*, 2020, **5**, 13076–13080.

47 R. Ramli and R. Hidayat, in *Graphene – A Wonder Material for Scientists and Engineers*, ed. M. Ikram, A. Maqsood and A. Bashir, IntechOpen, Rijeka, 2022, DOI: 10.5772/intechopen.107488.

48 S. Rostamnia, E. Doustkhah and B. Zeynizadeh, *Microporous Mesoporous Mater.*, 2016, **222**, 87–93.

49 J. Xu, M. Xu, J. Wu, H. Wu, W.-H. Zhang and Y.-X. Li, *RSC Adv.*, 2015, **5**, 72361–72368.
50 S. Rostamnia, E. Doustkhah and B. Zeynizadeh, *Microporous Mesoporous Mater.*, 2016, **222**, 87–93.
51 M. A. Zolfigol, M. Kiafar, M. Yarie, A. Taherpour and M. Saeidi-Rad, *RSC Adv.*, 2016, **6**, 50100–50111.
52 R. Ghorbani-Vaghei, Z. Toghraei-Semiromi and R. Karimi-Nami, *C. R. Chim.*, 2013, **16**, 1111–1117.